npj | materials degradation

Article

Published in partnership with CSCP and USTB

https://doi.org/10.1038/s41529-024-00456-8

Correlative, ML-based and non-destructive 3D-analysis of intergranular fatigue cracking in SAC305-Bi solder balls

Check for updates

Charlotte Cui[1], Fereshteh Falah Chamasemani[1], Priya Paulachan[1], Rahulkumar Sinojiya[1], Jördis Rosc[1], Michael Reisinger[2], Peter Imrich[2], Walter Hartner[3] & Roland Brunner[1]

Reliable connections of electrical components embody a crucial topic in the microelectronics and power semiconductor industry. This study utilises 3D non-destructive X-ray tomography and specifically developed machine learning (ML-) algorithms to statistically investigate crack initiation and propagation in SAC305-Bi solder balls upon thermal cycling on board (TCoB). We quantitatively segment fatigue cracks and flux pores from 3D X-ray tomography data utilising a multi-level ML-workflow incorporating a 3D U-Net model. The data reveals that intergranular fatigue cracking is the predominant failure mechanism during TCoB and that dynamic recrystallisation precedes crack initiation. Moreover, we find that fatigue cracks are initiated at surface notches, flux pores and printed circuit board-metallisation intrusions. The work provides important insights regarding the underlying microstructural and mechanical mechanisms for recrystallisation and cracking, uniting the aspects of big-data analysis with ML-algorithms and in-depth understanding about the underlying materials science.

The reliable connection of electrical components embodies a crucial topic in microelectronics and the power semiconductor industry. Hence, the intactness of a solder ball is crucial for the lifetime of the device and its functionality. The fundamental understanding of degradation mechanisms, in particular for more sustainable Pb-free solders remains a vital challenge in the field of materials science[1–5]. Solder balls serve as both electrical and thermal connections between the chip- and printed circuit board (PCB-) metallisations. Tin (Sn-) based solder alloys have largely replaced lead-based alloys in power- and microelectronics due to growing health and environmental concerns[6]. Sn – 3.0 wt.% Ag – 0.5 wt.% Cu (SAC305) is one of the most promising Sn-based solder alloys. However, conventional SAC solder balls can already exhibit microstructural degradation in the as-reflowed condition[7–9]. Flux pores may be formed during reflow due to outgassing of flux residues. These gasses can remain trapped within the solder after solidification and form spherical pores[8,9]. Moreover, the solder ball may also experience thermomechanical fatigue during service[10,11]. In operation, the current flow leads to resistive heating and further to multiple thermal loading when the device is repeatedly turned on and off. Mechanical stress emerges in the component due to the underlying coefficient of thermal expansion (CTE-) mismatches, originating from the multiple materials with various CTEs present in the device[11–13]. The SAC305 solder ball represents a mechanical weak spot within the device. Here, most of the generated deformation occurs due the low hardness of the β-Sn matrix of approximately 0.1 GPa[14]. The plastic strain thereby introduced into the solder material may lead to recovery, polygonization and recrystallisation[15]. Consequently, the initially single- or few-grained solder balls[15–17] undergo grain-refinement in highly strained areas. These highly strained areas are located in the proximity of the interfaces to the chip- and PCB-substrates, whereat shear strain is the predominant type of strain induced[11]. The new grain boundaries that are formed during recrystallisation in those high-strain areas serve as preferred crack propagation sites[10,11,15,18]. As a result, these intergranular fatigue cracks increase the thermal as well as the electrical solder resistivity and thereby impair the device's functionality and its lifetime[11,12].

The use of Bismuth (Bi) as an alloying element shows high potential to improve the thermo-mechanical stability of the SAC solder. The solubility limit of Bi in the β-Sn matrix of SAC-alloys is assumed to be around 2.5 wt.%[19]. Accordingly, when less than 2 wt.% Bi is added, it acts as solid solution strengthener in the β-Sn matrix[17,20]. As a solid solution strengthener, Bi elevates the yield stress of the solder[14,17,20] and thereby retards dynamic recrystallisation and the formation of new grain boundaries, i.e. reducing crack propagation sites. The utilisation of SAC305-Bi-alloys

[1]Materials Center Leoben Forschung GmbH, Roseggerstraße 12, 8700 Leoben, Austria. [2]Kompetenzzentrum für Automobil- und Industrieelektronik GmbH, Europastraße 8, 9524 Villach, Austria. [3]Infineon Technologies AG, Wernerwerkstraße 2, 93049 Regensburg, Germany. e-mail: roland.brunner@mcl.at

represents a very promising approach to diminish microstructural degradation and prolong the long-term fatigue stability of solder balls. A crucial component for the assessment of the relation between microstructural degradation and functionality is the need for characterisation of each solder ball volume on the ball grid array (BGA) in a statistical manner. Assessing entire solder ball volumes on BGAs produces large amounts of data which should be in keeping with the FAIR data principle[21].

Nevertheless, the failure assessment of a specific solder ball in complex BGA-geometries is often tedious, because daisy-chain measurements of electrical resistivity usually provide only information about the cumulative resistivity of all, or many, balls on the BGA. Such an approach does not reveal which particular ball has failed[11]. Light optical or electron microscopy techniques[16,22,23], on the other hand, require sample preparation for each and every ball and are therefore time-consuming and destructive. Furthermore, these techniques only give 2D-information of one particular cross-section, which may not be representative for the fatigue crack propagation in the solder ball volume. X-ray tomography eliminates these downsides as it allows non-destructive inspection of entire BGAs and delivers full 3D-information. Subsequent efficient image analysis is important to retrieve statistical information from the reconstructed 3D image data.

Image analysis incorporating supervised machine learning (ML) has proven to be significantly more efficient and accurate than manual feature segmentation[24,25]. In addition to the ability of ML-algorithms to process large amounts of image data, such as the ones produced with X-ray tomography, efficiently, algorithms are not subjected to volatile data evaluation noise as manual evaluation by human beings. Even data interpretation by the same person, and even the same expert, may underlie significant variability due to a number of day-dependent psychological factors[26]. This variability in human judgement may lead to inaccuracies in data evaluation, which are eliminated when mathematical algorithms are applied, not to mention the benefit of the possibility for automation. The development of ML-algorithms for image analysis has been rapidly evolving in recent years[24]. Convolutional neural networks (CNNs) have proven advantageous over manual image analysis, as they are able to build high-level features from low-level ones, providing accurate and efficient image recognition, object detection and image segmentation[24,25]. CNNs have been increasingly applied to medical and biological image analysis[25,27] and more recently, their use for image segmentation in materials science has been on the rise[28–36]. In microelectronics failure and reliability analysis, some work has been previously done on X-ray tomography data[37,38]. However, to our knowledge, the algorithms developed in these previous studies focus on the detection of flux pores. Although the CNN developed in[37] is trained on 3D data, its output is limited on a binary classification of solder balls with and without flux pores that are classified as "good" and "bad". On the contrary, the models developed in[38] perform the pore segmentation in two consecutive binary 2D segmentation steps: first, object detection of solders is carried out and subsequently, the pores are detected using the same binary approach. None of these previous studies apply a full three-dimensional segmentation to the X-ray tomography image data e.g. by a 3D U-Net architecture[39]. Moreover, the previous studies are constrained to image segmentation using CNNs without considering the underlying mechanisms for defect-formation and correlations with microstructural and mechanical phenomena in the material. Conversely, the implications for fatigue crack initiation by the segmented flux pores have not yet been considered. In short, the connection between ML-based image segmentation and materials science has not yet been made.

Therefore, our study intends to unite the aspects of statistical fatigue analysis and the underlying microstructural and stress-related mechanisms of fatigue crack initiation and propagation in SAC305-Bi solder balls, utilising 3D imaging with 3D ML-based image analysis. We quantitatively segment fatigue cracks and flux pores from 3D X-ray tomography data using a multi-level ML-workflow incorporating a 3D U-Net model. Moreover, we correlate the X-ray tomography data with microstructural features in the solder balls utilising high resolution field emission scanning electron microscopy (FESEM) and electron backscatter diffraction (EBSD). Further, we investigate the stress distribution within a solder ball during thermal cycling on board (TCoB) with finite element method (FEM) modelling. We draw connections between the simulated stress distribution, microstructural fatigue in the solder balls, i.e. recrystallisation and fatigue cracking, and statistical fatigue crack analyses from the ML-workflow. By bridging the gap between microstructural fatigue and its impact on statistically significant fatigue crack correlations, we elaborate on the importance of various small-scale mechanisms at play during TCoB. Whereat, we discuss that the rigorous understanding of the underlying small-scale mechanisms is crucial to avoid macroscopic failure within the electronic device. Based on the developed characterisation workflow we conclude that intergranular fatigue cracking is the predominant failure mechanism during TCoB and that dynamic recrystallisation precedes fatigue cracking. Moreover, we find that fatigue cracks are initiated at three kinds of notches, i.e. surface notches, flux pores and PCB-metallisation intrusions, and that crack propagation occurs along recrystallised grain boundaries which indicate copper enrichment.

Results

Visualisation of the BGA using correlated X-ray tomography and EBSD

The BGA package under investigation consists of solder balls sandwiched between the chip and PCB. Three SAC305-Bi solder alloys with different wt.% Bi (0, 1.1, 1.9) are subjected to prolonged thermal cycling in ambient atmosphere, see method section for further details. Here, thermal cycling on board (TCoB) is chosen to study the effect of mechanical stress on solder fatigue induced by CTE-mismatch, dynamic recrystallisation and Bi-content, regardless of electrical current. For each Bi-content, three BGAs with 152 balls each are investigated. After TCoB, the whole BGAs are non-destructively imaged in three-dimensions utilising X-ray tomography to gain sufficient statistical yield, see method section. An exemplary 3D reconstruction from the raw data of an investigated BGA is shown in Fig. 1a. The voxel size is $5.33 \times 5.33 \times 5.33\ \mu m^3$ and volume of interest shows the entire BGA (yellow), including the chip (blue) and PCB (brown), for all scans. The convention for the coordinate system used throughout the study is depicted in Fig. 1. Figure 1b shows the correlated x-y-, x-z- and y-z-views of the reconstructed 3D image from Fig. 1a. The bird-view of the BGA layout is visualised in the x-y-plane, whereas the two cross-sectional views are shown in the x-z-and y-z-plane indicating the elevation of the solder balls in z-direction. The locations of the individual intersections are illustrated in Fig. 1b by dashed lines. Degradation features of the solder balls such as the flux pores, fatigue cracks as well as the solder ball itself can be qualitatively identified due to different material densities present. Figure 1c shows an exemplary cross-sectional image in the x-z-plane for the 0, 1.1, 1.9 wt.% Bi-contents, alongside correlated FESEM EBSD overlays, see methods and Supplementary Note 6. The crystallographic information from the EBSD-maps allows the identification of crack propagation sites. The EBSD-maps depict the initial single- and few-grained crystal orientations of the individual solder balls, as well as the recrystallised areas which are induced by TCoB. The recrystallised areas are mainly concentrated in the vicinity of the substrate. Figure 1c qualitatively illustrates that the cracked proportion of the ball decreases with increasing Bi-content.

ML-based localisation and 3D segmentation of the BGA

For the thorough investigation of the degradation mechanisms present within the BGA-package, the statistical representativeness is a crucial and vital factor. Via the X-ray tomography characterisation, a large amount of volumetric data is generated, as further described in methods. The tomographic results can image, with a selected volume of interest, the entire BGA array with 152 solder balls in a non-destructive manner. Manual localisation and segmentation of each solder ball within the reconstructed three-dimensional image is of course highly labour-intensive, especially if the number of BGAs is more than one. Automation is the key here, however not trivial. Contrast- and brightness-gradients throughout the solder material, similar grey-values of cracks, pores and background as well as cracks

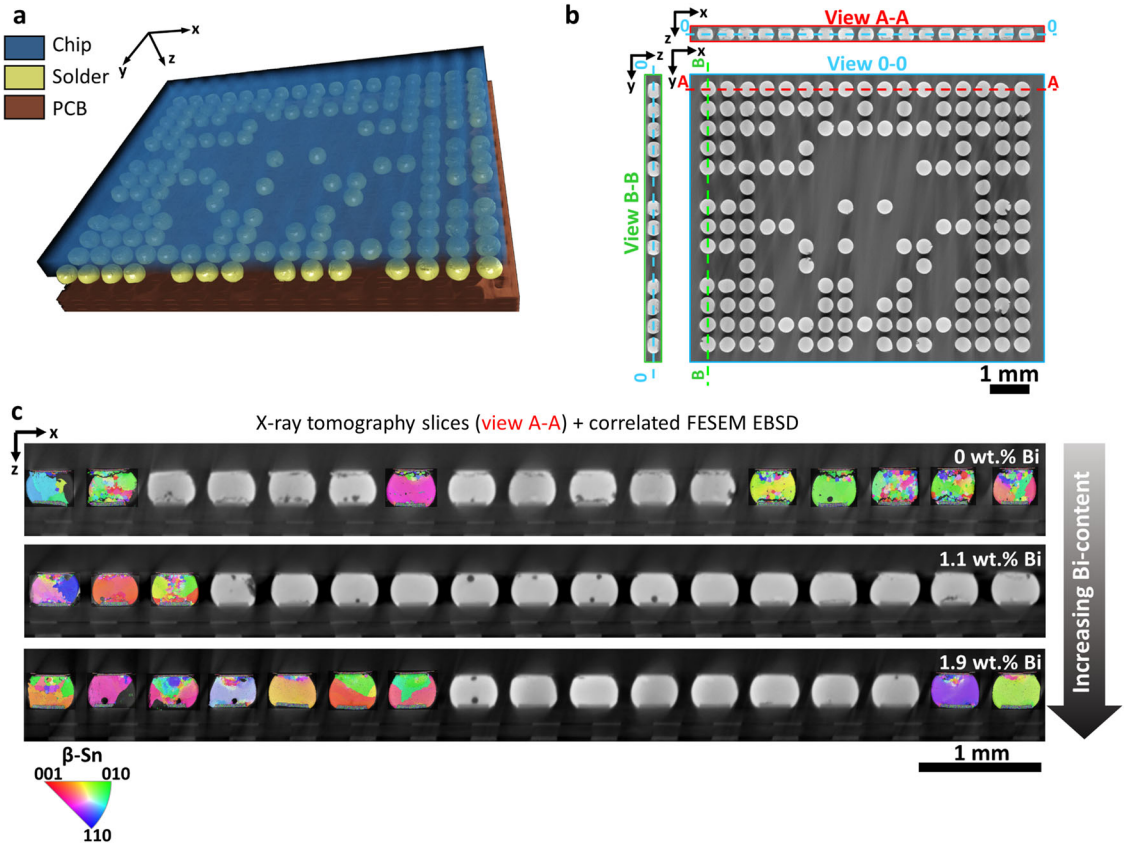

Fig. 1 | Correlated X-ray tomography and EBSD. a Rendered X-ray tomography image of the entire BGA with the chip (blue), the PCB (brown) and the solder balls (yellow). **b** X-ray tomography slice image of the BGA from the reconstructed three-dimensional raw data, for the x-y- (bird view), x-z- (cross-section 1) and y-z- (cross-section 2) planes. The locations of the cross-sections 1 and 2 are indicated by view A-A (red dashed line) and view B-B (green dashed line), respectively. For the location of the bird view a blue dashed line (0-0) is shown in cross-section (view A-A and view B-B). **c** Correlated cross-sectional X-ray tomography and FESEM EBSD maps for SAC305 with 0 wt.% Bi, 1.1 wt.% Bi and 1.9 wt.% Bi, respectively are presented. Grain orientation data from the FESEM EBSD characterisation is projected on the X-ray tomography data. The illustrated X-ray tomography cross-sections correspond to the view A-A.

propagating through pores and X-ray scattering artefacts at the solder surface make it difficult, if not impossible, to segment the features of interest merely via grey-value thresholding. To overcome this obstacle, an image processing workflow is developed utilising ML-algorithms capable of providing enhanced accuracy and efficiency. Figure 2a illustrates the multi-level image processing workflow, which consists of a localisation as well as a segmentation step. First, the localisation of solder balls in the X-ray tomography data is performed. A schematic of the model architecture is presented in Supplementary Fig. 1. Solder ball localisation is done in one x-y-slice with a sliding window-based binary CNN. The CNN generates bounding boxes for each solder ball as an output. An exemplary output from the localisation model is shown in Fig. 2a. The localisation model is trained on manually labelled 2D-data, which consists of 100 × 100 pixels^2 x-y-plane clips, either depicting a solder ball or not. Hence, the localisation model utilises a binary ansatz, which is trained on positive and negative image data, see methods for further details. The final training and validation accuracies for the localisation model are summarised in Table 1 and reach 100.00% and 99.25%, respectively. Further details about training, performance and validation of the ML-localisation model are presented in methods, Supplementary Note 1 and Supplementary Fig. 1, respectively.

After the localisation step, the segmentation of the solder balls is performed. The segmentation process consists of two deep learning 2D and 3D U-Net architectures. The 2D U-Net model is trained at first utilising the extracted bounding boxes from the localisation model, see methods and Supplementary Note 3. The architecture of the 2D U-Net is presented in Supplementary Fig. 1. A representative 2D U-Net segmentation result is shown in Fig. 2a for each Bi-content. Since the 2D U-Net performs the segmentation on one x-z-slice at a time, the outputted x-z-slices need to be re-assembled into the 3D ball volume for each ball. For the same reason, without consideration of previous or subsequent x-z-slices, the 2D U-Net may misclassify or over-segment cracks and pores or under-segment the Cu-metallisations, see also the evaluated model precision in Table 1 in this context. Hence, manual label refinement is further performed on the re-assembled segmentations from the 2D U-Net which are then utilised for training of the developed 3D U-Net. In order to ensure diversity in the training data, exemplary balls from each Bi-content are included in the training. Further details about the training, performance and validation of the 3D U-Net model are described in methods, Supplementary Fig. 1 and Supplementary Note 2, respectively.

Figure 2b exemplarily illustrates segmentation results obtained from the 3D U-Net model for each Bi-content as well as the normalised image data. The final step concerns the 3D reconstruction of the full BGA, shown in Fig. 2a, wherein each segmented ball is re-assigned its position according to the localisation outputs. We highlight the accuracy of the developed 3D segmentation method in Fig. 2b by comparing the segmentation results for representative solder balls utilising the 2D and 3D U-Net models. As illustrated, an accurate distinction between cracks and pores is not achieved by the 2D U-Net in non-trivial cases. The superiority of the 3D U-Net model is further highlighted by its ability for a fully automatic segmentation based on the voxel information, eliminating the need for the re-assembly of 2D segmentations, as well as its prediction precision on training-set independent data. Therein, the 2D U-Net segmentation model achieves a precision of 76.20%, whereas the 3D U-Net model reaches a precision of 91.90%, see Table 1. The 3D U-Net segmentation result provides enhanced possibilities

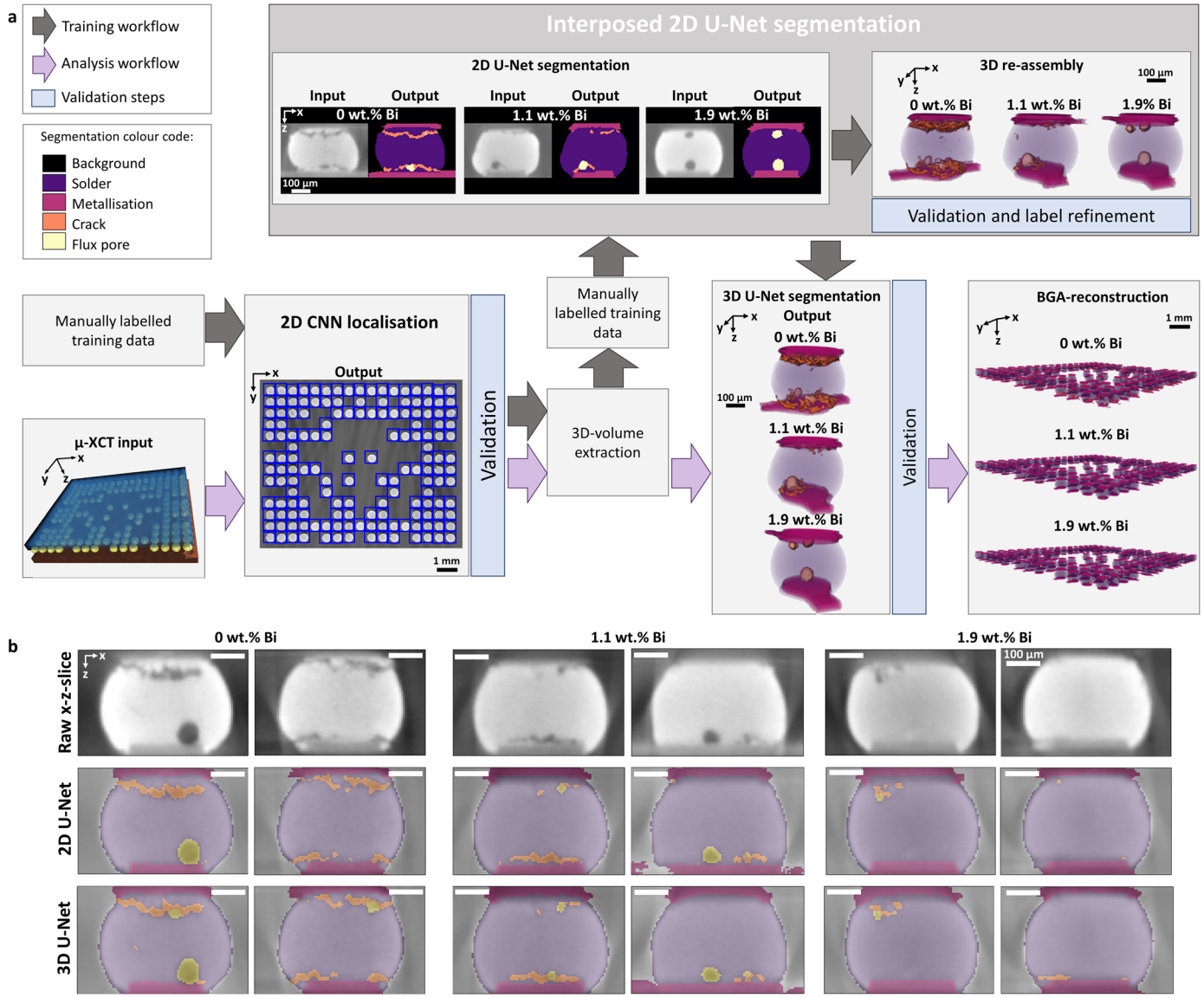

Fig. 2 | ML-based localisation and segmentation workflow. a ML-based segmentation workflow, illustrating both training (grey) and analysis (purple). Input is provided from the X-ray tomography data. First, a 2D localisation ML-model is trained to extract the positions of the solder balls in the x-y-plane. Second, the balls are extracted from the X-ray tomography using the generated bounding boxes from the ML-localisation model. For the training of the 2D U-Net segmentation model, tomography slices from the x-z-plane are manually labelled. Label refinement is performed on re-assembled x-z-slices obtained from the 2D U-Net segmentation model. The refined 2D-labels are further used as training data for the 3D U-Net segmentation model. In the final analysis workflow, raw 3D tomography data is used as an input, the 2D localisation performed, the individual solder balls are extracted based on the localisation, the 3D-segmentation is performed and the segmented balls are placed into the BGA-layout based on the localisation outputs. **b** Comparison of 2D U-Net and 3D U-Net segmentation results for representative solder balls with a Bi-content of 0, 1.1 and 1.9 wt.%, overlaid on the normalised raw tomography data. The segmentation colour code is the same as in a. Scale bar with 100 µm is valid for all images.

for further statistical analysis of the degraded solder balls in terms of the quantification of flux pore and fatigue crack volume, as well as the sites of fatigue crack initiation.

Crack initiation sites and visualisation of crack propagation

Here, the segmented morphological features in each ball, i.e. metallisations, cracks and flux pores, which are generated by the 3D U-Net model, are further utilised to gain a comprehensive insight into fatigue crack initiation and crack propagation after prolonged thermal cycling on board (TCoB). To that end, the segmented crack and pore labels are summed up and projected into the x-z- and x-y-plane, respectively. Whereby the resulting projections are performed for the chip- and PCB-side, separately, see Supplementary Note 4. Representative projections for each Bi-content after TCoB are illustrated in Fig. 3a, alongside with the 3D segmentations of the corresponding solder ball. The higher the intensity of the pixel value in the

Table 1 | Validation and training accuracies as well as model precisions for the utilised ML-based localisation and segmentation models

Model	Training Accuracy	Validation Accuracy	Model Precision
Localisation	100.00%	99.25%	100.00%
2D U-Net	99.60%	99.10%	76.20%
3D U-Net	99.40%	99.40%	91.90%

Training and validation accuracy as well as model precision.

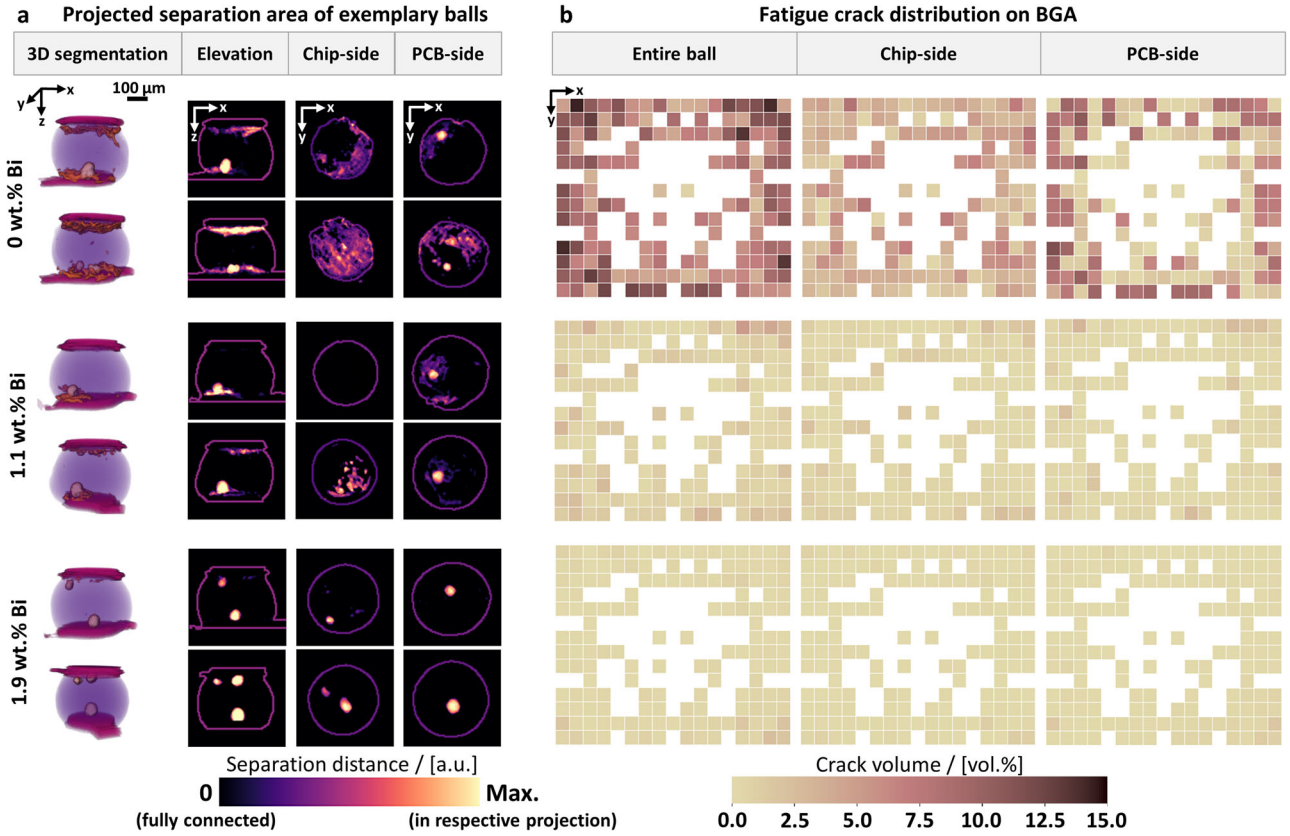

Fig. 3 | Separation distance and visualisation of the crack volume distribution on the entire BGA. a From left to right: Representative 3D segmentations, accumulated crack- and pore-projections in x-z and x-y (chip- and PCB-sides) planes for each Bi content with the respective outlines of the solder bulk. The brighter the pixel in the respective projection, the larger the separation distance between the adjacent solder-surfaces along the projection axis in the given position. Scale bar with 100 µm is valid for all images. **b** Heatmaps of the crack volumes of the entire BGAs for the different Bi-contents of 0 (first row), 1.1 (second row) and 1.9 (third row) wt.%, respectively. Each square represents a single solder ball on the BGA. The darker the square, the larger the crack volume in the corresponding ball.

projections, the larger is the separation distance of the solder–to–solder surfaces. For a better evaluation of the fatigue crack initiation sites, the corresponding outlines of the solders as well as the metallisations are also illustrated in the x-z-projections. The outlines of the solder bulk near the interfaces are overlaid on the x-y-projections. The overlays of the respective outlines visualise the progression of the fatigue cracks with regards to the solder. Zero intensity (black) within these outlines represents fully connected solder material, whereas zero-values outside of the outlines correspond to the background. Two mechanisms can be identified with respect to crack initiation and propagation from the obtained data. It becomes apparent from the generated x-z-projections, that cracks on the chip-side start from a notch-like geometry feature at the solder surface and propagate inward, as can be seen in the x-y-projections. Furthermore, the x-y-projections indicate that cracks can also be initiated at flux pores, i.e. from internally formed notches, as illustrated in the x-y-projections of the 1.1 wt.% Bi balls.

For the quantification of the crack propagation on the entire BGA, we calculate the percentages of the crack volume (CV) in relation to the solder ball volume for each ball. The crack volume is extracted from the segmented voxels associated with the crack. In Fig.3b, BGA-heatmaps of the CV, calculated from the segmented X-ray tomography data are shown for the entire ball, the chip- as well as for the PCB-side, for different Bi-contents. With these heatmaps, the crack volume of the individual solder balls can be evaluated on BGA level based on the colour shading. This approach provides a measure of the crack propagation within each individual ball after TCoB. This illustration can be easily interpreted by humans and can be incorporated into quality and reliability control for a fast identification of badly fatigued solder balls. Based on the heatmaps and quantified crack volume percentage, solder balls can be selected and further prepared for high resolution characterisation, e.g. cross-sectional SEM analysis. The heatmaps in Fig. 3b of the 0 wt.% Bi solder reveal that the fatigue crack distribution is rather homogeneous on the chip-side, compared to a more inhomogeneous distribution for the crack volume in the PCB-side. For the 1.9 wt.% Bi balls, the crack volume is rather low for the entire BGA, as illustrated by the shading in the heatmap of Fig. 3b. The approach for the construction of the presented heatmaps is further described in Supplementary Note 4.

Statistical analysis of the evaluated morphological and geometric features

To find the primary causes for the solder fatigue, we further statistically analyse the segmented morphological features, i.e. metallisations, cracks and flux pores, to find correlations for the fatigue of solder balls. In Fig.4a, we investigate for different Bi-contents the relationship between the crack volume (CV) and the flux pore volume (PV) not only for the entire ball, but also separately for the chip- and PCB-side. Moreover, Spearman correlation coefficients (r) are calculated for each Bi-content. The statisticaly relevant CV correlations are summarised in Table 2. Overall, the balls with 0 wt.% Bi exhibit a higher CV than the solder balls with 1.1 and 1.9 wt.%, as also illustrated in Fig. 3b. We argue, according to the observations, that crack initiation may originate from notches induced by the geometry of the package, as well as by the flux pores within the solder ball. The scatter plots in Fig. 4a show the CV – PV relationships. It can be seen that overall, flux pores on the PCB-side are larger than pores on the chip-side. However, the CVs in the entire ball show sign-related inconsistencies in their r-values when they are correlated with PV. Therefore, we split the statistical analyses into chip- and PCB-sides for a more thorough investigation. Further details can be extracted from the Spearman correlation coefficients. The correlation coefficients in Fig. 4a and Table 2 show a weak positive correlation for pores

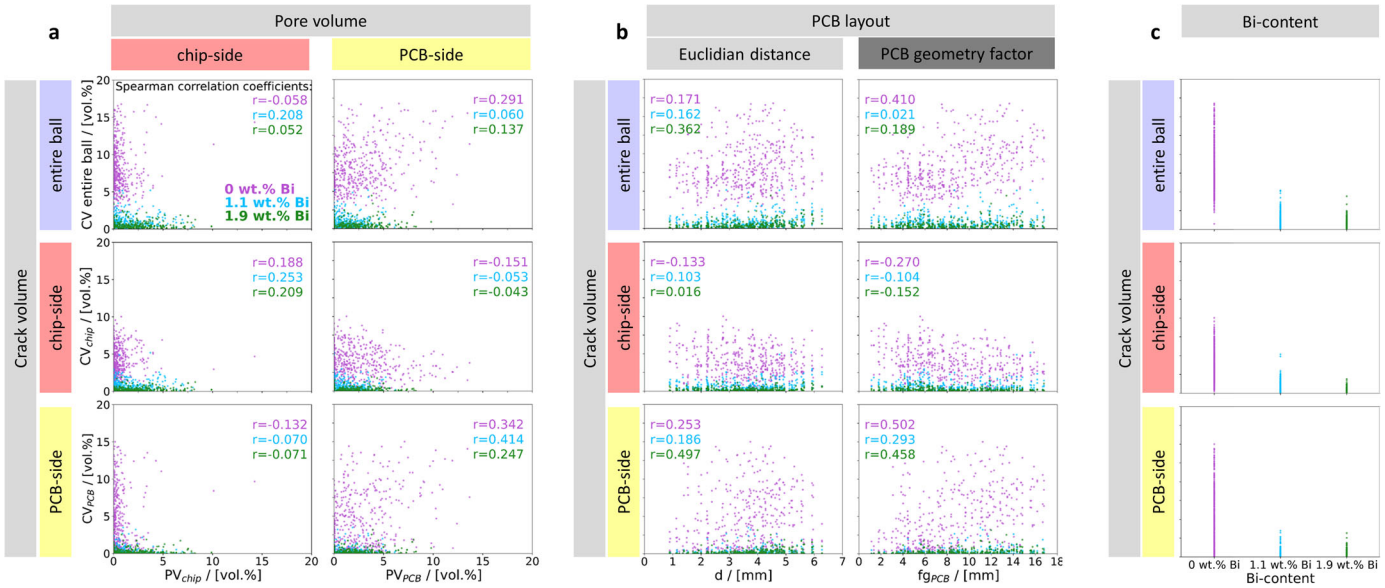

Fig. 4 | Statistical analysis of the morphological and geometric features for the entire solder ball, chip- and PCB-side. Statistical analysis of the crack volume (CV) and its correlation with various solder ball properties for the various Bi-contents with 0 wt.% (pink), 1.1 wt.% (blue) and 1.9 wt.% (green). The Spearman correlation coefficients (r) are calculated for each Bi-content. All properties are correlated for the CV in the entire ball, as well as for the chip- and PCB-side separately. **a** Correlation for different Bi-contents between the CV of the entire ball, chip-side (CV_{chip}) and PCB-side (CV_{PCB}) with the: flux pore volumes on the chip-side (PV_{Chip}) and flux pore volumes on the PCB-side (PV_{PCB}), from left to right. **b** Correlation for different Bi-contents between CV of the entire ball, CV_{chip} and CV_{PCB} with the: Eucledian distance of the ball centre from the BGA centre (d) and PCB-geometry-factor (f_{gPCB}), from left to right. **c** Correlation between the CV of the entire ball, CV_{chip} and CV_{PCB} with: different Bi-contents (0, 1.1 and 1.9 wt.%).

on the same side as the crack. Therefore, it is assumed that flux pores impact fatigue crack initiation in solder balls by acting as internal notches. Conversely, the correlations are negative for pores on the opposite side of the crack which indicates a decreased probability for crack initiation on the opposing side of a pore.

Considering the BGA-layout and under the assumption of isotropic thermal expansion of the multi-material substrates, solder balls located farther from the BGA-centre experience higher stresses during TCoB. Hence, fatigue of solder balls may have progressed faster for balls further away from the centre, since they experience larger stresses during TCoB compared to balls close to the centre. Therefore, we plot the Euclidean distance of the ball centre from the BGA-centre (d) vs. CV and the PCB-geometry-factor (f_{gPCB}) vs. CV. The correlations of the crack volume with the Euclidean distance of the ball centre from the BGA-centre (d) are shown in Fig. 4b. The overall crack volume correlates positively with increasing distance. However, the correlations of cracks on the chip-side with d show sign-related inconsistencies between the Bi-contents. The cracks on the PCB-side, on the other hand, correlate positively with increasing distance d. Since the PCB-copper (Cu) metallisations intrude into the solder ball, as can be seen in the segmentations in Fig. 2 and Fig. 3, and since Cu is much stiffer than the solder ball, the PCB-routes may act as additional notches in the solder. Therefore, the number of PCB-routes leading away from each ball are incorporated in the analysis, in addition to the BGA-centre distance. This relationship is described by the PCB-geometry-factor, calculated as $f_{gPCB} = (1 + n_{PCBroutes}) \cdot d$, where $n_{PCB\text{-}routes}$ denotes the number of PCB-routes leading to the ball. CV_{chip} correlates negatively with f_{gPCB}, whereas CV_{PCB} correlates positively, see Table 2. Hence, it is assumed that the combined effect of PCB-intrusions and centre-distance plays a significant role in the fatigue crack initiation and propagation in solder balls on the PCB-side.

Lastly, Fig. 4c shows that all 0 wt.% Bi balls are cracked to some extent, whereas some balls with 1.1 wt.% and 1.9 wt.% are still fully intact after TCoB. The maximum CV_{chip} decreases parabolically with increasing Bi-content, while the maximum CV_{PCB} does not significantly decrease between the 1.1 wt.% and 1.9 wt.% Bi balls, see Fig. 4c. The Spearman correlation coefficients for the CV of the entire ball –, CV_{chip}– and CV_{PCB} – property relationships are presented in Supplementary Tables 1, 2 and 3, respectively.

Table 2 | Spearman correlation coefficients for the crack volume – property relationships

Bi-content	r (CV_{chip} – PV_{chip})	r (CV_{chip} – PV_{PCB})	r (CV_{PCB} – PV_{chip})	r (CV_{PCB} – PV_{PCB})	r (CV_{PCB} – f_{gPCB})
0 wt.%	0.188	-0.151	-0.132	0.342	0.502
1.1 wt.%	0.253	-0.053	-0.070	0.414	0.293
1.9 wt.%	0.209	-0.043	-0.071	0.247	0.458

Here, the statistically significant correlations between crack volume (CV) and solder properties are listed. CV_{chip} – PV_{chip}, CV_{PCB} – PV_{PCB} and CV_{PCB} – f_{gPCB} exhibit positive correlation coefficients, whereas CV_{chip} – PV_{PCB} and CV_{PCB} – PV_{chip} correlate negatively.

Stress distribution, recrystallisation and intergranular cracking

We simulate the stress-distribution within the solder ball during TCoB by using ANSYS MAPDL 2022R2. Here, we utilise the geometry data obtained from the X-ray tomography, see Supplementary Note 5 and method section. Since the stiffness of the Cu-metallisations is much higher than that of the solder, the metallisations are represented as fixed nodes at the top and bottom of the ball. The metallisation intrusion from the PCB is implemented with the properties of Cu. The 3D and 2D geometries used for FEM are shown in Fig. 5a. The plane of the 2D-geometry is shown in grey in the 3D-geometry. Simulation results for the β-Sn matrix are shown, during exposure to a TCoB-cycle with a temperature increase from -40 °C to 125 °C and a subsequent cooling to −40 °C. Both ramp- and dwell-times are set to 15 minutes, respectively. The parameters of the simulated thermal cycle correspond to the ones from the real TCoB-testing conditions. The simulation results for one exemplary TCoB-cycle are shown in Supplementary Fig. 2. The highest stress in the solder is present near the interfaces to the substrates, since the effects of CTE-mismatch are most pronounced here. More specifically, the stresses are concentrated at the surface notches on the chip-side and the notches created by the intrusion of the PCB-metallisation into the solder. It can also be seen that the ball-shape of the solder causes an hourglass-shaped stress distribution over the solder cross-section.

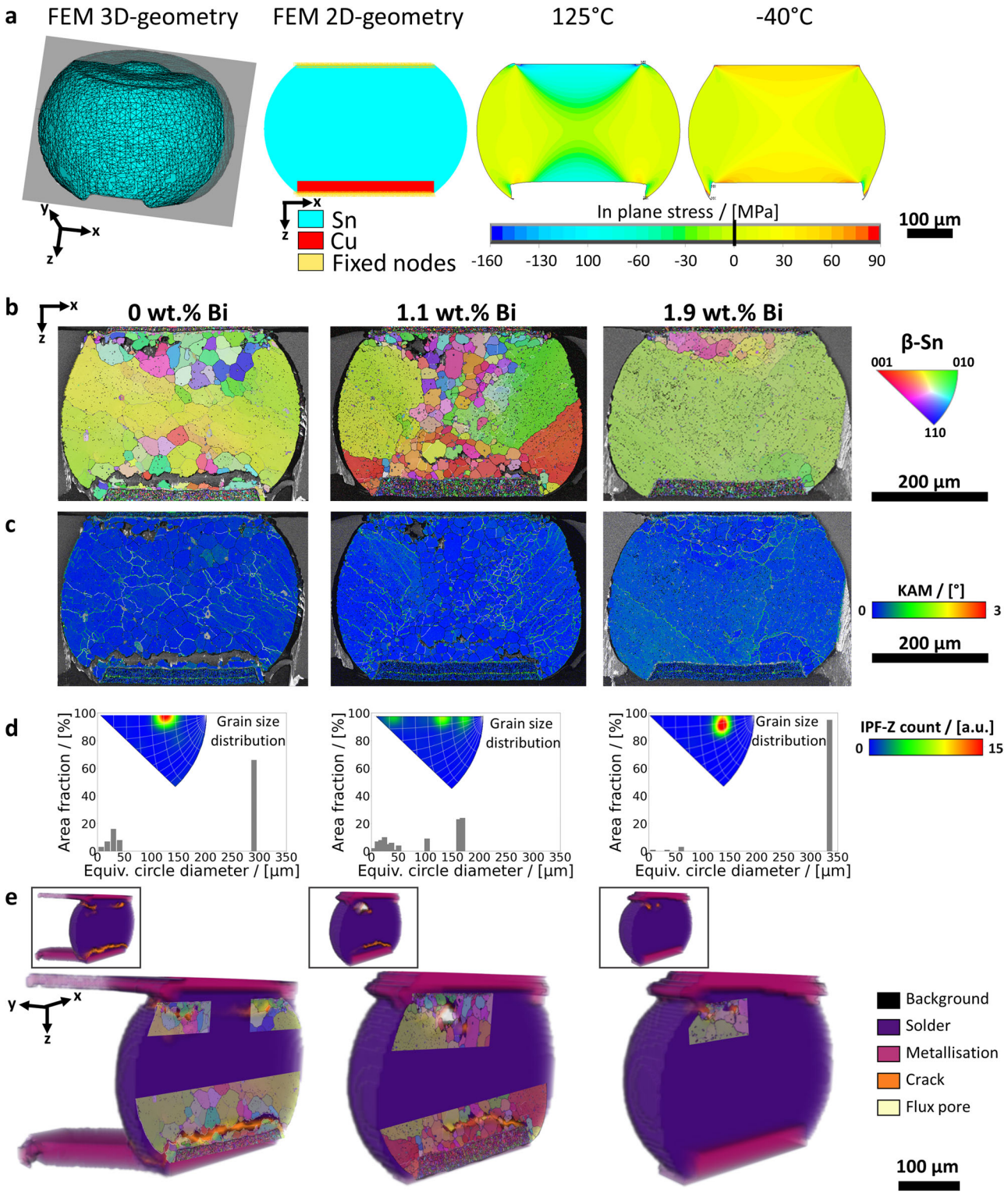

Fig. 5 | Microstructure characterisation and FEM. FEM geometry, FEM stress distribution during TCoB, cross-sectional FESEM EBSDs, IPFs, grain size distributions and correlation of EBSD-maps with ML-based 3D-segmentation. **a** FEM geometry (3D and 2D) and stress distribution in the solder ball cross-section during one exemplary TCoB-cycle. The plane of the 2D-geometry is shown in grey in the 3D-geometry. Simulated stress distributions for 125 and -40 °C are exemplarily demonstrated for the 2D cross-section. Colour bar is scaled from -160 MPa (blue) to 90 MPa (red). Scale bar with 100 µm for all images. **b** Cross-sectional EBSD-maps for representative solder balls, one for each Bi-content. Scale bar with 200 µm for all images. **c** KAM-maps for 0 wt.%, 1.1 wt.% and 1.9 wt.% Bi. Scale bar with 200 µm for all images. **d** IPFs and grain size distributions for the EBSD-maps illustrated in **b**. **e** The EBSD-maps are correlated with the respective 3D segmentations. Scale bar with 100 µm for all images.

As fatigue crack propagation impairs the remaining functionality of the solder during TCoB, the propagation paths of those cracks are of interest. In order to visualise these crack propagation paths within the solder microstructure, cross-sectional FESEM EBSD scans are performed for representative solder balls with different Bi-contents. Hourglass-shaped recrystallisation fronts in the initially single- or few-grained balls are visible in the EBSD-maps, see Fig. 5b. This is in keeping with the simulated stress distribution shown in Fig. 5a, as recrystallisation will occur in the highly stressed (strained) areas first. Moreover, the EBSD-maps in Fig. 5b show that recrystallisation starts at the surface-notches on the chip-side and the metallisation intrusion on the PCB-side, which matches the stress concentrations in those areas seen in the FEM modelling results. In the recrystallised areas near the interfaces, intergranular cracks can be seen in the 0 wt.% Bi sample. The same is true for the 1.1 wt.% Bi sample, although the intergranular crack seen there is less gaping than in the 0 wt.% Bi sample. The 1.9 wt.% Bi sample only exhibits a small crack at the chip-interface, but it does also show the hourglass-shaped recrystallisation front, albeit in much earlier stages than the 0 wt.% Bi and the 1.1 wt.% Bi samples. In order to understand the effect of Bi-additions in the solder microstructure after TCoB, FESEM EDX analysis is done for exemplary regions for each Bi-content, see Supplementary Note 7 and Supplementary Fig. 4. No primary Bi-precipitates can be seen for either alloy.

Figure 5c depicts the kernel average misorientation (KAM-) maps for the respective EBSD-maps in Fig. 5b. From the KAM-maps, high-strain areas in the solder cross-sections can be qualitatively deduced. Recrystallised areas appear less strained than single-crystalline regions. In Fig. 5d we present the inverse pole figures (IPFs) for the y-direction and the grain size distributions for each cross-section. The IPFs appear smeared out, indicating distorted orientations around the initial crystal orientation(s) of the balls. In order to correlate the fatigue cracks from the 3D segmentation with their propagation paths in the solder microstructure, exemplary EBSD-maps are overlaid with corresponding X-ray tomography segmentations in Fig. 5e. The correlated overlays clearly reveal that the cracks visible in the segmented X-ray tomography data are indeed intergranular fatigue cracks. Hence, the 3D ML-analysis based on X-ray tomography data uncovers the intergranular fatigue crack propagation in the solder balls. Not only does the developed ML-segmentation workflow allow a fully automated, non-destructive 3D failure analysis of entire BGAs, but the underlying microstructural and mechanical mechanisms for fatigue crack initiation and propagation are also correlatively established.

Discussion

The functionality of a solder ball in terms of its ability to conduct both electrical and thermal current from the chip to the PCB is vastly impaired when the material is interrupted by gas-filled volumes such as flux pores and fatigue cracks[11]. Hence, the non-destructive, statistically significant failure analysis of fatigue crack initiation and propagation in solder balls is essential. Furthermore, an in-depth understanding of the underlying mechanisms for solder fatigue on the microstructural scale is crucial for the design of materials science-informed engineering solutions to prolong the fatigue lifetime of lead-free solder balls.

We statistically identify the solder properties that impact fatigue in solder balls from 3D data by conducting non-destructive X-ray tomography and applying sophisticated ML-based image analysis methods. The statistical results show a significant prolongation of solder ball lifetime by the addition of Bi to the SAC305 alloy. In order to understand the underlying mechanisms of solder fatigue, we discuss (1) the impact of the periodical stress and strain on the solder during TCoB, (2) the crack propagation through the solders and (3) the influence of Bi on the fatigue and microstructural properties of SAC305 solder balls.

Due to the CTE-mismatches in the multi-component device, mechanical stress and deformation are induced in the solder during TCoB[15,40]. Since stress and deformation occur periodically during TCoB, the predominant mechanisms of solder degradation are considered to be fatigue and the propagation of fatigue cracks into the solder balls. Figure 3a and Fig. 5b support this assumption and illustrate the initiation of cracks either at surface notches or at internal notches, i.e. metallisation intrusions and flux pores, and their propagation into the solder bulk, a typical characteristic of fatigue cracks[41]. As the mechanical stress in the solder during TCoB stems from CTE-mismatches between the various components of the multi-layer device, stress and strain are most pronounced near the interfaces to the chip and the PCB. The emerging inhomogeneous stress distribution is even more enhanced by the presence of surface-notches and the intrusion of the PCB-metallisation into the ball. The accompanied FEM simulation illustrates how the ball-shape of the solder translates the shear stress at the interfaces into an hourglass-shaped stress gradient within the ball, see Fig. 5a. This stress gradient induces a proportional strain gradient in the solder, consisting of both plastic and elastic strain. Accordingly, the dislocation density is higher near the interfaces and notches, causing the solder to dynamically recover and recrystallise there earlier compared to the rest of the solder. This hourglass-shaped recrystallisation behaviour is observed in the EBSD-maps in Fig. 5b. Further, the EBSD-maps show that the solidification structures of the balls are initially built of either single crystals or a few large grains. These observations are consistent with the findings in[15,20,22]. The IPFs in Fig. 5d show that the orientations of the newly formed grains are smeared out around the initial crystal orientation. Hence, the solder balls in this study do not undergo primary recrystallisation, where statistically oriented grains would nucleate in a highly deformed crystal[41]. Rather, continuous recovery and polygonization take place in the investigated solder balls, as rearrangement of dislocations generates small-angle grain boundaries and new grains that are slightly misoriented towards the initial crystal orientation. Furthermore, highly strained regions in the initial single crystals, visible in the KAM-maps in Fig. 5c, are likely to undergo recrystallisation with continued cycling. The KAM-distributions are also in agreement with the FEM simulations in Fig. 5a. Additional EBSD- and KAM-maps, as well as IPFs are shown in Supplementary Fig. 3 to support the provided argumentation. Since the Cu PCB-metallisation is much stiffer than the solder, its intrusion into the ball acts as an additional internal notch and crack initiation site. The notch effect of the PCB-intrusion is confirmed by the FEM-simulations in Fig. 5a as well as by the EBSD-maps in Fig. 5b, where polygonization can be seen to start in the vicinity of the PCB-intrusions. This can be seen particularly clearly in the EBSD-map of the 1.9 wt.% Bi sample.

The correlation of the EBSD-maps with the corresponding 3D segmented image data in Fig. 5e confirms that the cracks visualised with X-ray tomography and analysed with the ML-assisted workflow are indeed intergranular fatigue cracks. Since the cracks propagate along recrystallised grain boundaries, those are of particular interest for the understanding of fatigue crack propagation. EDX analyses of exemplary grain boundaries for each Bi-content are shown in Supplementary Fig. 4. The EDX-maps show Cu-enrichment along recrystallised grain boundaries. This enrichment may promote intergranular fatigue cracking. Since grain boundaries are first formed in the high-strain areas near the solder interfaces, intergranular crack initiation and propagation are also expected to start there. The onset of dynamic recrystallisation, and therefore the formation of grain boundaries, requires a critical dislocation density. For Bi-concentrations below the solubility limit in the β-Sn matrix of about 2.5 wt.%[19], Bi is expected to be soluble in the matrix. Once the solubility limit is exceeded, primary Bi-precipitates would form during solidification from the melt during reflow, as observed in previous studies[17,20,42,43]. With Bi-precipitates present in the matrix, the microstructural and mechanical properties of the alloy would change entirely. To ensure that there are no primary Bi-precipitates present in the matrix, high-magnification EDX-maps are acquired, see Supplementary Fig. 4. As no primary Bi-precipitates are present, it is assumed that Bi is solved in the β-Sn matrix, acting as a solid solution strengthener and increasing the Sn-matrix' yield strength. Since the primary fatigue symptom is intergranular crack propagation, as illustrated in Fig. 5b, Bi is therefore expected to delay both recrystallisation and subsequent intergranular fatigue cracking. This can be seen in Fig. 1c and Fig. 5e, where cross-sectional overview of EBSD-maps of exemplary balls for 0 wt.%, 1.1 wt.% and 1.9 wt.%

Bi samples are correlated with the X-ray tomography slices and 3D segmentations, respectively. This relationship is also shown in the scatter plots in Fig. 4. Moreover, the IPFs in Fig. 5d and Supplementary Fig. 3 are more localised around the initial crystal orientation(s) in the 1.9 wt.% Bi balls compared to the 0 wt.% Bi balls which indicates that dynamic recrystallisation is further advanced in 0 wt.% Bi balls. Furthermore, fatigue cracking has progressed further in balls with decreasing Bi-content, which is also in keeping with the results from the statistical analyses shown in Fig. 4. As already mentioned, the solid solution strengthening effect of Bi delays polygonization, grain boundary formation and subsequent intergranular fatigue cracking in Bi-containing solder balls. Nonetheless, the 1.1 wt.% and 1.9 wt.% Bi samples are also recrystallised to various extents. However, intergranular cracks have not propagated to the same proportion as in the 0 wt.% Bi samples, as can be seen in Fig. 1c and Fig. 5b, despite the grain boundaries also being enriched with Cu, illustrated in Supplementary Fig. 4. Therefore, it is assumed that Bi-additions may also influence the structure of grain boundaries in SAC305, leading to strengthening of the recrystallised grain boundaries. The study of structure and elemental composition of grain boundaries in Bi-free and Bi-containing solder balls is not part of this work but will be the subject of a future study. Conversely, cracks, once initiated in a ball, dampen the stress from the substrates so it cannot be efficiently transmitted to the opposing side of the crack. Accordingly, no more, or fewer, dislocations are produced in the ball and dynamic recrystallisation stops, or slows down, once a crack is initiated, since the dislocation density and rearrangement of dislocations into an energetically more favourable configuration is its driving force. Hence, recrystallisation in the 0 wt.% Bi ball in Fig. 5b is less progressed than in the 1.1 wt.% Bi sample, as the cracks in the 0 wt.% Bi ball inhibit further recrystallisation after crack initiation and the strain energy from further cycling is invested in propagating the cracks. Apparently, however the recrystallised grains in the 0 wt.% Bi sample have undergone coarsening during the high-temperature periods of TCoB after cracking. This results in larger grains compared to the 1.1 wt.% and 1.9 wt.% Bi samples, as shown in the grain size distributions in Fig. 5d. Moreover, the KAM-maps in Fig. 5c show that strain is less pronounced in polygonised areas of the cross-section, compared to the initial grain. Therefore, it is assumed that recrystallisation provides stress relief in the solder. This thorough microstructural analysis, in combination with the FEM modelling results, elaborates the underlying mechanisms for fatigue cracking. Moreover, the correlations of the EBSD-maps with X-ray tomography data and their segmentations prove the validity of our statistical analysis of solder fatigue.

Several conclusions can be drawn from our study on solder fatigue, its statistical correlations with solder ball properties and the underlying microstructural and mechanical mechanisms. Firstly, intergranular cracks propagating along recrystallised grain boundaries of solder balls constitute the predominant fatigue mechanism during thermal cycling of BGAs. The grain boundaries indicate Cu-enrichment. Secondly, recrystallisation and grain boundary formation in high-strain areas near the chip- and PCB-interfaces of the solder balls precedes crack initiation. The stress distribution in the solder ball during TCoB is simulated with FEM and it is in keeping with the shape of the recrystallisation fronts in EBSD-maps. Thirdly, fatigue cracks initiate either at notches at the solder ball surface, Cu-metallisation intrusions or at internal defects, i.e. flux pores, and propagate along recrystallised grain boundaries into the surrounding solder ball matrix. These aspects could be considered in the design of BGAs to engineer the notch-effects on solder fatigue. Lastly, alloying Bi to SAC305 markedly delays recrystallisation, fatigue crack initiation and propagation, thereby prolonging the lifetime of solder balls. EDX-maps show that the investigated Bi-concentrations act as solid solution strengthener in β-Sn rather than forming primary precipitates, thereby increasing the solder ball's yield strength.

In summary, this study proves non-equivocally that intergranular fatigue cracks and flux pores in SAC305 + x Bi (x = 0, 1.1, 1.9 wt.%) solder balls can be visualised with 3D X-ray tomography and statistically analysed with the ML-algorithms developed for this purpose. The ML-based segmentation workflow developed in this study can be used to efficiently and non-destructively inspect solder balls on BGA-level with high statistical yield. The developed workflow provides the possibility for efficient and advanced failure analysis. The gained data reveals the crack initiation at surface notches and at internal notches, i.e. flux pores and PCB-metallisation intrusions, a typical feature of fatigue cracks. Further, intergranular propagation paths of the fatigue cracks represent a major issue. The work provides important insights regarding the underlying mechanisms for recrystallisation and crack propagation, as well as the effects of Bi on the microstructural fatigue in the solder alloys. The analysis of microstructural features and the simulation of the stress distribution is utilised to understand the statistically evaluated solder fatigue, thereby uniting the aspects of big-data analysis with ML-algorithms and in-depth understanding about the underlying materials science.

Methods

The experimental and methodological approaches of this study are described in the following. More details can be found in the Supplementary Notes.

Sample Production and TCoB

Three solder materials are investigated: Sn – 3.0 wt.% Ag – 0.5 wt.% Cu (SAC305), SAC305 + 1.1 wt.% Bi and SAC305 + 1.9 wt.% Bi. Bi acts as a solid-solution strengthener in β-Sn. No primary precipitation of Bi is expected for this content[17,20]. The investigated solder balls are produced by droplet spraying in an inert N_2 atmosphere and subsequently soldered between the Cu-metallisations of the chip and the PCB. Reflow is done at a peak temperature of 240 °C and with a mean heating rate of 44 °C/min in inert N_2 atmosphere, followed by rapid air cooling to 90 °C with a mean cooling rate of 107 °C/min and ambient air cooling to room temperature. The 3D BGA layout is shown in Fig. 1a, alongside with its coordinate system for the subsequent analysis. Figure 1b shows the x-y-layout of the BGA. Thermal cycling is conducted between −40 and 125 °C with ramp- and dwell-times of 15 mins, respectively. Hot and cold air is alternately injected into a furnace in order to obtain heating rates as linear as possible. The furnace temperature during thermal cycling is homogenised by air circulation. The 0 wt.% Bi sample is thermally cycled for 1764 cycles, the 1.1 wt.% Bi samples and the 1.9 wt.% Bi samples for 2914 and 2570 cycles, respectively. The BGAs with Bi-content underwent larger numbers of cycles, since the amount of Bi-additions provide solid solution strengthening effects of the β-Sn matrix and hence delay recrystallisation and subsequent intergranular cracking.

Non-destructive 3D X-ray tomography scans

Non-destructive X-ray tomography has the capability to scan entire BGAs in less than an hour. Hence, this method is suitable for the generation of the large amount of image data that is necessary for ML and statistical statements regarding solder fatigue. The X-ray tomography scans are done with a GE Phoenix Nanotom M (research edition) using a cone beam configuration. By using a cone beam, the achievable magnification is limited by the lateral size of the BGA (~10 × 7 mm^2). The achievable voxel-size results to 5.33 × 5.33 × 5.33 μm^3 for scanning entire BGAs. The interaction of an X-ray beam with matter is described by the Beer-Lambert-law:

$$\frac{I}{I_0} = \exp\left(-\frac{\mu}{\rho}\rho\, d\right), \tag{1}$$

where I denotes the transmitted X-ray intensity, I_0 the incident X-ray intensity, $\frac{\mu}{\rho}$ the attenuation coefficient, ρ the material density and d the penetrated sample thickness. Due to the dependency of X-ray attenuation on the density, more specifically the atomic number, of the penetrated material, air-filled defects, i.e. cracks and pores, appear darker in the X-ray tomography scans than β-Sn and Cu-metallisations. This allows the distinction of pores and cracks based on their grey-values.

FESEM EBSD

FESEM overview EBSD maps are used to verify X-ray tomography imaging, i.e. to assess whether its resolution is sufficient for the investigation of solder fatigue. Moreover, EBSD maps provide crystallographic information about the solder balls. The final solder ball cross-sections for EBSD are prepared with a Hitachi IM4000+ ion-slicer, which yields deformation-free surfaces. The accelerating voltage for ion-slicing is set to 6 kV and the swing angle to 30° with 3 swings per minute. Overview EBSD-maps are acquired with a Zeiss 450 Gemini FESEM. An accelerating voltage of 10 kV, a step size of 400 nm and an Oxford Symmetry detector are used for EBSD-mapping. Oxford Instrument AZtecCrystal 5.1 is used for the evaluation of EBSD data. IPFs are used to extract information about the polygonization behaviour of the solder balls and grain size distributions are plotted in order to determine their recrystallisation stage. Neighbouring grains with misorientations >10° are considered in the grain size distributions. Since the polygonised grains are quasi-circular, their equivalent circle diameter is used as size metric. The grain size distribution is plotted as the area-weighted fraction of grains with a particular diameter in proportion to the entire solder cross-section. More details can be found in Supplementary Note 6.

Data generation and pre-processing

Due to the large amount of 3D-image data produced by X-ray tomography, supervised ML-algorithms are used for the quantitative image analysis. The reconstructed 3D dataset of each solder ball consists of $96 \times 96 \times 96$ voxels^3 in x, y and z direction. Overall, 1368 datasets were generated and further analysed. Within the pre-processing step from X-ray tomography, the raw-files of the collected 2D projections are extracted with the VG Studio MAX software. The X-ray tomography data is aligned in the 3D space before the raw-files are exported. In order to overcome contrast variances between the various scans, the raw image data is normalised within the pre-processing step utilising the Python OpenCV 4.0.1 package, before it is inputted in the ML-workflow. The subsequent ML-analysis is done in two steps: x-y-localisation followed by 3D feature segmentation.

ML-based localisation

The localisation algorithm is based on a binary, sequential, feed-forward sliding-window convolutional neural network (CNN) adapted from[30]. The model is trained on manually labelled 2D-data, which consists of 100×100 pixels^2 x-y-plane clips. In total, 1208 (628 positive + 580 negative) images are used for the training. The localisation model is trained for 40 epochs with a learning rate of 10^{-3} using Python 3.8.13, tensorflow 2.9.1, keras 2.9.0, Adam optimiser and a binary cross-entropy loss function on an Intel Core i5-8265U CPU with 16 GB RAM. Its schematic architecture is shown in Supplementary Fig. 11 and described in detail in Supplementary Note 1, alongside with exemplary training images, the model's accuracy and loss histories as well as its testing accuracy.

ML- based segmentation

The 3D segmentation model is based on a U-Net CNN. The 3D segmentation model is built from the Python library segmentation models 3D[2]. It is trained with keras 2.8.0, tensorflow 2.8.2, Python 3.9.16, and scikit-learn 1.2.1 for 300 epochs, using softmax activation functions, categorical cross entropy loss functions and the Adam optimiser with learning rate of 10^{-4} on a NVIDIA A40 GPU with 48GB RAM. 3D volumes from the raw µ-XCT data are utilized, which contain the entire solder ball. For the training data 61 manually refined $96 \times 96 \times 96$ voxels^3 re-assembled outputs from the 2D segmentation model are used as training data, whereby the test size is 5%. Further details about the architecture, training and validation accuracy and loss histories are depicted in detail in Supplementary Fig. 1 and Supplementary Note 2. In order to efficiently generate a large amount of training data for the 3D segmentation model, a 2D segmentation U-Net model is used. The 2D U-Net model is trained on 4992 manually labelled 96×96 pixels^2 slices (x-z-plane), with a test size of 20% utilising the extracted bounding boxes from the localisation model, see also Supplementary Note 3. The training data for the 2D segmentation model is manually labelled using ilastik 7.1.0[44]. Here, the model is trained for 200 epochs on a NVIDIA A40 GPU with 48GB RAM. Further details with respect to the architecture, training and validation accuracy and loss histories of the 2D segmentation model are provided in Supplementary Fig. 1 and Supplementary Note 3. For the visualisation of the segmented image data we utilise Avizo.

Calculation of separation distance and crack distribution on the BGA

In order to visualise the crack initiation sites in the solder balls, the segmented cracks and pores obtained from the 3D U-Net are projected into 2D-planes, i.e. x-z- and x-y-projections. The respective voxels, associated with either cracks or pores, are summed up along the y-axis for the x-z-projections and along the z-axis for the x-y-projections. Additionally, the outlines of the solder ball and metallisations are thresholded and overlaid onto the projections.

The visualisation of the crack volume distribution on the BGA utilising heatmaps allows fast identification of particularly badly fatigued solder balls based on the quantified crack volume percentage. To that end, the crack volumes gained from the 3D segmentation are put into relation with the solder volume to obtain the volume percentage of cracks in the respective balls. These crack volume proportions are then schematically plotted into heatmaps which exhibit the BGA-layout. This is done by utilising the localisation outputs.

FEM simulation

During TCoB, mechanical stresses are introduced into the solder balls. These mechanical stresses stem from misfits in CTE between the various components in the multi-material device. In order to visualise the stress distribution in the solder ball, 3D FEM simulations were done with Ansys MAPDL 2022R2 for one exemplary heating and cooling cycle, considering the 2D plane in the centre of the 3D geometry, see Supplementary Note 5. The 3D geometry is extracted from an .stl file from X-ray tomography imaging. The geometry and the results of the FEM simulation are shown in Fig. 5a and in Supplementary Fig. 2. The simulated heating cycle is implemented with the same parameters as the TCoB cycling done in this study: Heating from −40 °C to 125 °C, followed by cooling to −40 °C. Both the ramp times and dwell times are set to 15 minutes, respectively. A thermal transient analysis is carried out based on the heating cycle. The temperature profile of the FEM simulation is shown in Supplementary Fig. 2, alongside cross-sectional in plane stress distributions for a selection of timesteps. The elastic tensor of β-Sn and the thermal expansion coefficient are taken from[45]. Boundary conditions for the FEM analysis are implemented considering the following. Firstly, the surface notches on the chip-side are represented by fixed nodes, which account for the attachment of the ball to the chip-metallisation. The PCB-metallisation intrusion is implemented with the mechanical and thermal expansion values of Cu from[46]. Lastly, like the chip-side, the bottom nodes of the metallisation are rigidly fixed. More details about the FEM simulation are given in Supplementary Note 5.

Data availability

The data that support the findings of this study are available from the corresponding author upon reasonable request.

Code availability

All code that support the findings of this study are available from the corresponding author upon reasonable request.

Received: 18 January 2024; Accepted: 15 March 2024;
Published online: 20 April 2024

References

1. Bieler, T. R., Jiang, H., Lehman, L. P., Kirkpatrick, T. & Cotts, E. J. Influence of Sn Grain Size and Orientation on the Thermomechanical Response and Reliability of Pb-free Solder Joints, 1462–1467; https://doi.org/10.1109/ECTC.2006.1645849 (2008).

2. Chung, C. K., Duh, J.-G. & Kao, C. R. Direct evidence for a Cu-enriched region at the boundary between Cu6Sn5 and Cu3Sn during Cu/Sn reaction. *Scr. Mater.* **63**, 258–260 (2010).
3. Gong, J., Conway, P. P., Liu, C. & Silberschmidt, V. V. Heterogeneous intragranular inelastic behavior of a Sn-Ag-Cu Alloy. *J. Elec Mater.* **38**, 2429–2435 (2009).
4. Huang, Y. L., Lin, K. L. & Liu, D. S. Microstructure evolution and microimpact performance of Sn–Ag–Cu solder joints under thermal cycle test. *J. Mater. Res.* **25**, 1312–1320 (2010).
5. Kariya, Y., Williams, N., Gagg, C. & Plumbridge, W. Tin pest in Sn-0.5 wt.% Cu lead-free solder. *JOM* **53**, 39–41 (2001).
6. Cheng, S., Huang, C.-M. & Pecht, M. A review of lead-free solders for electronics applications. *Microelectron. Reliab.* **75**, 77–95 (2017).
7. Kelly, M. B., Niverty, S. & Chawla, N. Four dimensional (4D) microstructural evolution of Cu6Sn5 intermetallic and voids under electromigration in bi-crystal pure Sn solder joints. *Acta Materialia* **189**, 118–128 (2020).
8. Dudek, M. A. et al. Three-dimensional (3D) visualization of reflow porosity and modeling of deformation in Pb-free solder joints. *Mater. Charact.* **61**, 433–439 (2010).
9. Jiang, L., Chawla, N., Pacheco, M. & Noveski, V. Three-dimensional (3D) microstructural characterization and quantification of reflow porosity in Sn-rich alloy/copper joints by X-ray tomography. *Mater. Charact.* **62**, 970–975 (2011).
10. Korhonen, T.-M. K., Lehman, L. P., Korhonen, M. A. & Henderson, D. W. Isothermal fatigue behavior of the near-eutectic Sn-Ag-Cu alloy between −25 °C and 125 °C. *J. Elec Mater.* **36**, 173–178 (2007).
11. Depiver, J. A., Mallik, S. & Amalu, E. H. Effective solder for improved thermo-mechanical reliability of solder joints in a Ball Grid Array (BGA) Soldered on Printed Circuit Board (PCB). *J. Elec Mater.* **50**, 263–282 (2021).
12. M. Brunnbauer, T. Meyer, G. Ofner, K. Mueller, R. Hagen. Embedded Wafer Level Ball Grid Array (eWLB). *33rd International Electronics Manufacturing Teclmology Conference*, 1–6 (2008).
13. Jiang, Q., Deshpande, A. & Dasgupta, A. Effects of Anisotropic Viscoplasticity on SAC305 Solder Joint Deformation: Grain-scale Modeling of Temperature Cycling. In *2021 22nd International Conference on Thermal, Mechanical and Multi-Physics Simulation and Experiments in Microelectronics and Microsystems (EuroSimE)* (IEEE2021), pp. 1–4.
14. Hu, S.-H. et al. Effects of bismuth additions on mechanical property and microstructure of SAC-Bi solder joint under current stressing. *Microelectron. Reliab.* **117**, 114041 (2021).
15. Henderson, D. W. et al. The microstructure of Sn in near-eutectic Sn–Ag–Cu alloy solder joints and its role in thermomechanical fatigue. *J. Mater. Res.* **19**, 1608–1612 (2004).
16. Holdermann, K., Cuddalorepatta, G. & Dasgupta, A. Dynamic recrystallization of Sn3.0Ag0.5Cu Pb-Free Solder alloy. In *Dynamic Recrystallization of Sn3.0Ag0.5Cu Pb-Free Solder Alloy* (ASMEDC2008), pp. 163–169.
17. Huang, M. L. & Wang, L. Effects of Cu, Bi, and In on microstructure and tensile properties of Sn-Ag-X(Cu, Bi, In) solders. *Met. Mat. Trans. A* **36**, 1439–1446 (2005).
18. Bieler, T. R. et al. The role of elastic and plastic anisotropy of Sn in recrystallization and damage evolution during thermal cycling in SAC305 solder joints. *J. Electron. Mater.* **41**, 283–301 (2012).
19. Sayyadi, R. & Naffakh-Moosavy, H. The role of intermetallic compounds in controlling the microstructural, physical and mechanical properties of Cu-Sn-Ag-Cu-Bi-Cu solder joints. *Sci. Rep.* **9**, 8389 (2019).
20. Chantaramanee, S. & Sungkhaphaitoon, P. Influence of bismuth on microstructure, thermal properties, mechanical performance, and interfacial behavior of SAC305-xBi/Cu solder joints. *Trans. Nonferrous Met. Soc. China* **31**, 1397–1410 (2021).
21. Boeckhout, M., Zielhuis, G. A. & Bredenoord, A. L. The FAIR guiding principles for data stewardship: fair enough? *Eur. J. Hum. Genet. : EJHG* **26**, 931–936 (2018).
22. Ben Romdhane, E., Guédon-Gracia, A., Pin, S., Roumanille, P. & Frémont, H. Impact of crystalline orientation of lead-free solder joints on thermomechanical response and reliability of ball grid array components. *Microelectron. Reliab.* **114**, 113812 (2020).
23. Du, Y. et al. TEM and EBSD characterization revealing the recrystallization process occurring in the Sn-3.0Ag-0.5Cu Ball Grid Array solder joints during thermal cycling. *Mater. Charact.* **200**, 112890 (2023).
24. LeCun, Y., Bengio, Y. & Hinton, G. Deep learning. *Nature* **521**, 436–444 (2015).
25. Yao, X., Wang, X., Wang, S.-H. & Zhang, Y.-D. A comprehensive survey on convolutional neural network in medical image analysis. *Multimed. Tools Appl.* **81**, 41361–41405 (2022).
26. Kahneman, D., Sibony, O. & Sunstein, C. R. *Noise. A Flaw in Human Judgment* (Little, Brown Spark, New York, 2021).
27. Ronneberger, O., Fischer, P. & Brox, T. U-Net: Convolutional Networks for Biomedical Image Segmentation.
28. Vorauer, T. et al. Impact of solid-electrolyte interphase reformation on capacity loss in silicon-based lithium-ion batteries. *Commun. Mater*. **4**; https://doi.org/10.1038/s43246-023-00368-1 (2023).
29. Wijaya, A. et al. Multi-method characterization approach to facilitate a strategy to design mechanical and electrical properties of sintered copper. *Mater. Des.* **197**, 109188 (2021).
30. Paulachan, P., Siegert, J., Wiesler, I. & Brunner, R. An end-to-end convolutional neural network for automated failure localisation and characterisation of 3D interconnects. *Sci. Rep.* **13**, 9376 (2023).
31. Furat, O. et al. Machine learning techniques for the segmentation of tomographic image data of functional materials. *Front. Mater*. **6**; https://doi.org/10.3389/fmats.2019.00145 (2019).
32. Han, Y. et al. Center-environment feature models for materials image segmentation based on machine learning. *Sci. Rep.* **12**, 12960 (2022).
33. Masubuchi, S. et al. Deep-learning-based image segmentation integrated with optical microscopy for automatically searching for two-dimensional materials. *npj 2D Mater Appl* **4**; https://doi.org/10.1038/s41699-020-0137-z (2020).
34. Akers, S. et al. Rapid and flexible segmentation of electron microscopy data using few-shot machine learning. *npj Comput. Mater.* **7**; https://doi.org/10.1038/s41524-021-00652-z (2021).
35. Choudhary, K. et al. Recent advances and applications of deep learning methods in materials science. *npj Comput. Mater.* **8**; https://doi.org/10.1038/s41524-022-00734-6 (2022).
36. Torbati-Sarraf, H. et al. Machine-learning-based algorithms for automated image segmentation techniques of transmission X-ray Microscopy (TXM). *JOM* **73**, 2173–2184 (2021).
37. Hsu, P.-N. et al. Artificial intelligence deep learning for 3D IC reliability prediction. *Sci. Rep.* **12**, 6711 (2022).
38. Pahwa, R. et al. Deep Learning Analysis of 3D X-ray images for automated object detection and attribute measurement of buried package features, 221–227; https://doi.org/10.1109/EPTC50525.2020.9315043.
39. Solovyev, R., Kalinin, A. A. & Gabruseva, T. 3D convolutional neural networks for stalled brain capillary detection. *Comput. Biol. Med.* **141**, 105089 (2022).
40. Deshpande, A., Kaeser, H. & Dasgupta, A. Effect of stress state on fatigue characterization of SAC305 solder joints. In *2019 20th International Conference on Thermal, Mechanical and Multi-Physics Simulation and Experiments in Microelectronics and Microsystems (EuroSimE)* (IEEE2019), pp. 1–3.
41. Haasen, P. *Physikalische Metallkunde*. 3rd ed. (Springer, Berlin Heidelberg, 1994).

42. Belyakov, S. A. et al. Precipitation and coarsening of bismuth plates in Sn–Ag–Cu–Bi and Sn–Cu–Ni–Bi solder joints. *J. Mater. Sci.: Mater. Electron* **30**, 378–390 (2019).
43. Cai, C., Xu, J., Wang, H. & Park, S. B. A comparative study of thermal fatigue life of Eutectic Sn-Bi, Hybrid Sn-Bi/SAC and SAC solder alloy BGAs. *Microelectron. Reliab.* **119**, 114065 (2021).
44. Berg, S. et al. ilastik: interactive machine learning for (bio)image analysis. *Nat. Methods*; https://doi.org/10.1038/s41592-019-0582-9 (2019).
45. The Materials Project. Materials Explorer: Sn (mp-55), database version v2022.10.28. https://doi.org/10.17188/1267399. Available at https://next-gen.materialsproject.org/materials/mp-55?_limit=75&formula=Sn#how_to_cite (2020).
46. Ross, R. B. *Metallic Materials Specification Handbook*. 4th ed. (Ross Materials Technology Ltd, East Kilbride, Glasgow, 1992).

Acknowledgements

The authors gratefully acknowledge the financial support under the scope of the COMET program within the K2 Center “Integrated Computational Material, Process and Product Engineering (IC-MPPE)” (Project No 886385). This program is supported by the Austrian Federal Ministries for Climate Action, Environment, Energy, Mobility, Innovation and Technology (BMK) and for Labour and Economy (BMAW), represented by the Austrian Research Promotion Agency (FFG), and the federal states of Styria, Upper Austria and Tyrol, P. No. P2.22 ECOSolder. We acknowledge the support from J. Wosik for the EBSD and EDX measurements and B. Sartory for fruitful discussions regarding EBSD and EDX experiments.

Author contributions

C.C. performed under the supervision of R.B. the image-and data-analysis work and the data interpretation and evaluation. R.S. performed the simulations. F.F. developed and trained the U-Net models. P.P. and C.C. developed the localisation model under supervision of R.B. W.H. fabricated and provided the samples, with support from M.R. and P.I. R.B. and C.C. planned the FESEM-EBSD, FESEM-EDX and X-ray tomography measurements. J.R. performed the X-ray tomography measurements and reconstructed the data. C.C. and R.B. wrote the paper. All authors discussed the results and commented on the paper.

Competing interests

The authors declare no competing interests.

Additional information

Supplementary information The online version contains supplementary material available at https://doi.org/10.1038/s41529-024-00456-8.

Correspondence and requests for materials should be addressed to Roland Brunner.

Reprints and permissions information is available at http://www.nature.com/reprints

Publisher’s note Springer Nature remains neutral with regard to jurisdictional claims in published maps and institutional affiliations.

Open Access This article is licensed under a Creative Commons Attribution 4.0 International License, which permits use, sharing, adaptation, distribution and reproduction in any medium or format, as long as you give appropriate credit to the original author(s) and the source, provide a link to the Creative Commons licence, and indicate if changes were made. The images or other third party material in this article are included in the article’s Creative Commons licence, unless indicated otherwise in a credit line to the material. If material is not included in the article’s Creative Commons licence and your intended use is not permitted by statutory regulation or exceeds the permitted use, you will need to obtain permission directly from the copyright holder. To view a copy of this licence, visit http://creativecommons.org/licenses/by/4.0/.

© The Author(s) 2024